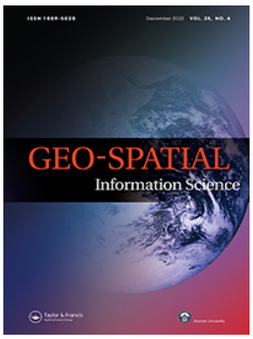

Geo-spatial Information Science

ISSN: (Print) (Online) Journal homepage: https://www.tandfonline.com/loi/tgsi20

Displacements of Fushun west opencast coal mine revealed by multi-temporal InSAR technology

Lianhuan Wei, Fang Wang, Cristiano Tolomei, Shanjun Liu, Christian Bignami, Bing Li, Donglin Lv, Elisa Trasatti, Yuan Cui, Guido Ventura, Meng Ao, Stefano Salvi, Shiliu Wang & Xingyu Pan

To cite this article: Lianhuan Wei, Fang Wang, Cristiano Tolomei, Shanjun Liu, Christian Bignami, Bing Li, Donglin Lv, Elisa Trasatti, Yuan Cui, Guido Ventura, Meng Ao, Stefano Salvi, Shiliu Wang & Xingyu Pan (2023): Displacements of Fushun west opencast coal mine revealed by multi-temporal InSAR technology, Geo-spatial Information Science, DOI: 10.1080/10095020.2023.2239285

To link to this article: https://doi.org/10.1080/10095020.2023.2239285

Published online: 02 Aug 2023.

GEO-SPATIAL INFORMATION SCIENCE
https://doi.org/10.1080/10095020.2023.2239285

Displacements of Fushun west opencast coal mine revealed by multi-temporal InSAR technology

Lianhuan Wei[a], Fang Wang[a], Cristiano Tolomei[b], Shanjun Liu[a], Christian Bignami[b], Bing Li[c], Donglin Lv[d], Elisa Trasatti[b], Yuan Cui[c], Guido Ventura[b,e], Meng Ao[a], Stefano Salvi[b], Shiliu Wang[a] and Xingyu Pan[a]

[a]School of Resources and Civil Engineering, Northeastern University, Shenyang, China; [b]National Earthquake Center, Istituto Nazionale di Geofisica Vulcanologia, Roma, Italy; [c]Department of Geological Environment Monitoring, Liaoning 10th Geological Brigade, Fushun, China; [d]Energy Geology Institute, Liaoning Geology and Mineral Resources Group, Shenyang, China; [e]Istituto per lo Studio degli impatti Antropici e Sostenibilità in ambiente marino (IAS), Consiglio Nazionale delle Ricerche, Capo Granitola (TP), Genova, Italy

ABSTRACT

In this paper, the Multi-Temporal Interferometric Synthetic Aperture Radar (MT-InSAR) technology is adopted to monitor the Line of Sight (LOS) displacement of Fushun West Opencast Coal Mine (FWOCM) and its surrounding areas in northeast China using Sentinel-1 Synthetic Aperture Radar (SAR) images acquired from 2018 to 2022. The spatial-temporal evolution of urban subsidence and the south-slope landslide are both analyzed in detail. Comparison with ground measurements and cross-correlation analysis via cross wavelet transform with monthly precipitation data are also conducted, to analyze the influence factors of displacements in FWOCM. The monitoring results show that a subsidence basin appeared in the urban area near the eastern part of the north slope in 2018, with settlement center located at the intersection of E3000 and fault F1. The Qian Tai Shan (QTS) landslide on the south slope, which experienced rapid sliding during 2014 to 2016, presents seasonal deceleration and acceleration with precipitation, with the maximum displacement in vicinity of the Liushan paleochannel. The results of this paper have fully taken in account for the complications of large topographic relief, geological conditions, spatial distribution and temporal evolution characteristics of surface displacements in opencast mining area. The wide range and long time series dynamic monitoring of opencast mine are of great significance to ensure mine safety production and geological disaster prevention in the investigated mining area.

ARTICLE HISTORY
Received 25 January 2023
Accepted 15 July 2023

KEYWORDS
Multi-Temporal InSAR (MT-InSAR); opencast mine; landslide; land subsidence; cross wavelet transform

1. Introduction

Coal is the pillar energy resource supporting global economic activities due to its low price, abundant availability and wide distribution, which accounts for more than 30% of the energy consumption worldwide and 65% in China (Asif et al. 2015; Park et al. 2017). Opencast mining is a classical operation mode of large coal mines worldwide thanks to its high-efficiency and low-cost advantages (Chaulya and Prasad 2016; Dash 2019; Wu et al. 2020). With the increase of coal production and continuous excavation in opencast mines, many huge deep mining pits and loose piles of waste deposits are formed (Mu et al. 2022; Sellier et al. 2021; Yang et al. 2016). Because of the long-term carving and the complicated geological conditions, catastrophic landslides frequently occur in opencast mines, bringing significant safety threats to mining production operations (Feng et al. 2019; Nguyen, Tien, and Do 2020; Ouyang et al. 2018; Sun et al. 2022). Therefore, it is of vital significance to perform continuous displacement monitoring of opencast mines and their surroundings (Loupasakis et al. 2014; Onder and Mutlu 2017).

Fushun West Opencast Coal Mine (FWOCM), located in the southwest of Fushun city, is the largest opencast coal mine in Asia (Nie et al. 2015). Due to the long-term intensive mining activities, over 100 landslides and severe urban subsidence have been reported in FWOCM, directly threatening the safety of neighboring residents, factories and other infrastructures (Sun et al. 2022). Till now, various in-situ monitoring devices have been widely assembled on the unstable slopes of FWOCM, such as continuous Global Navigation Satellite Systems (GNSS) receivers, total stations, tiltmeters, inclinometers, stress gauges and prism leveling, etc. (Li et al. 2015; Nie et al. 2017; Yan et al. 2013; Zhang et al. 2019; Zhou et al. 2022). Unfortunately these on-site observation techniques suffer from the disadvantages of high-cost, heavy workload, low efficiency and sparse point density (Samsonov, d'Oreye, and Smets 2013; Wang et al. 2022). Up until now, it is still infeasible to

CONTACT Cristiano Tolomei cristiano.tolomei@ingv.it

continuously evaluate the long-term displacements of the whole mining area in FWOCM with these on-site monitoring techniques.

In recent decades, with the continuous enrichment of satellite Synthetic Aperture Radar (SAR) data resources, the Multi-Temporal Interferometric Synthetic Aperture Radar (MT-InSAR) technique has become a fundamental tool to estimate surface displacements with high spatial resolution and millimeter accuracy (Ferretti et al. 2011; Hooper 2008; Hooper, Segall, and Zebker 2007; Lanari et al. 2004; Mora, Mallorqui, and Broquetas 2003). MT-InSAR detects pixels exhibiting long-term coherence and estimates displacements of such pixels by phase time series analysis (Osmanoğlu et al. 2016; Rosen et al. 2000). It has been widely adopted to monitor displacements of multiple geohazards induced by natural phenomena and anthropogenic activities (Dong et al. 2018; Orellana et al. 2022; Orhan et al. 2021; Papageorgiou et al. 2019; Yang et al. 2020). Despite the wide application of MT-InSAR, unfortunately it is seldom adopted to monitor the long-term displacements of FWOCM in recent decades. He et al analyzed the initiation of Qian Tai Shan (QTS) landslide during 2007–2010 by adopting Small BAseline Subset (SBAS) on ALOS PALSAR data (He et al. 2015). However, quantitative monitoring on the recent spatial-temporal evolution of displacements in FWOCM is still unavailable.

Targeting at revealing the recent spatial temporal evolution of displacements in FWOCM, we adopted the MT-InSAR technique on Sentinel-1 images, and further analyzed the influence factors of instability. In addition, we conducted cross wavelet transform (XWT) on the MT-InSAR observations and precipitation data. The results showed that precipitation was correlated with slope deformation, demonstrating that precipitation was an important factor in inducing landslides.

2. Study area

2.1. Geological settings

Fushun West Opencast Coal Mine (FWOCM), located in the southwest of Fushun city, is the largest opencast coal mine in Asia (Nie et al. 2015). After continuous mining of 120 years since 1901, a huge mining pit extending 6.6 km in E-W and 2.2 km in N-S direction has formed, with maximum depth of approximately 418 m and spatial coverage of 10.8593 km^2, as shown in Figure 1 (Liu et al. 2022; Zhou et al. 2022). The Fushun urban area is in vicinity of FWOCM, with many industrial plants and residential buildings surrounding it. Due to the long-term intensive mining activities, over 100 landslides have been reported in FWOCM, directly threatening the safety of neighboring residents, factories and other infrastructures (Sun et al. 2022). The multiple huge landslides happened on the north slope of FWOCM forced abandonment and relocation of the former oil plant and thermal power plant, resulting in tremendous economic losses (Figure 2). The most dangerous landslide in FWOCM is the Qian Tai Shan (QTS) landslide on the south slope, which is a huge translational landslide extending 3.1 km in E-W and 1.5 km in N-S direction, with height difference of approximately 500 m, as shown by the green dashed lines in Figure 1(b). Development of the QTS landslide was initiated in the early 2010s when some small cracks appeared, and experienced four years' rapid movement during 2013 to 2016, with maximum downslope displacements of approximately 90 m. The long-term mining activities have also led to complicated subsidence and structural deterioration of buildings in Fushun city, leading to relocation of thousands of residents.

From the regional perspective, FWOCM is located in Hunhe fault zone, which is the northern extension of Tanlu fault zone, resulting in very complex regional geological settings. The Hunhe fault zone comprises several nearly parallel reverse faults extending in E-W direction in Fushun city, among which F1 and F1A are the two major faults. The geological structure of FWOCM is mainly controlled by Fushun compound syncline, which comprises several syncline folds arranged in an oblique manner, with the axial direction extending in NE 75°. The strata of the compound syncline in the west are inverted, which gradually return to normal in the east. The faults in FWOCM are mainly a group of faults (including F1 and F1A) distributed in parallel along the NEE direction, which are characterized by thrust. Other faults are mainly near S-N faults and N-W faults associated with these faults and controlled by the same stress field. The structure of the south slope is also very complicated, with many longitudinal and transverse faults. Fault F2 on the south slope is a normal fault with E-W trending. The QTS landslide body is located above fault F2, with lower boundary mostly located in the exposed zone of fault F2. Fault F5 is located on the east boundary of the QTS landslide, which is a tension torsion normal fault with NW-SE trending. Besides, there are also several small faults associated with F5 along N-S direction on the south slope. The types of the bedrock in the mining area are quite diverse. The sedimentary rock stratum is mainly composed of mudstone and shale, which are both soft rocks. And, the soft rock stratum is covered by granite gneiss and volcanic rocks.

2.2. Datasets and instruments

In this study, the Sentinel-1 images in interferometric TOPSAR acquisition mode covering FWOCM are

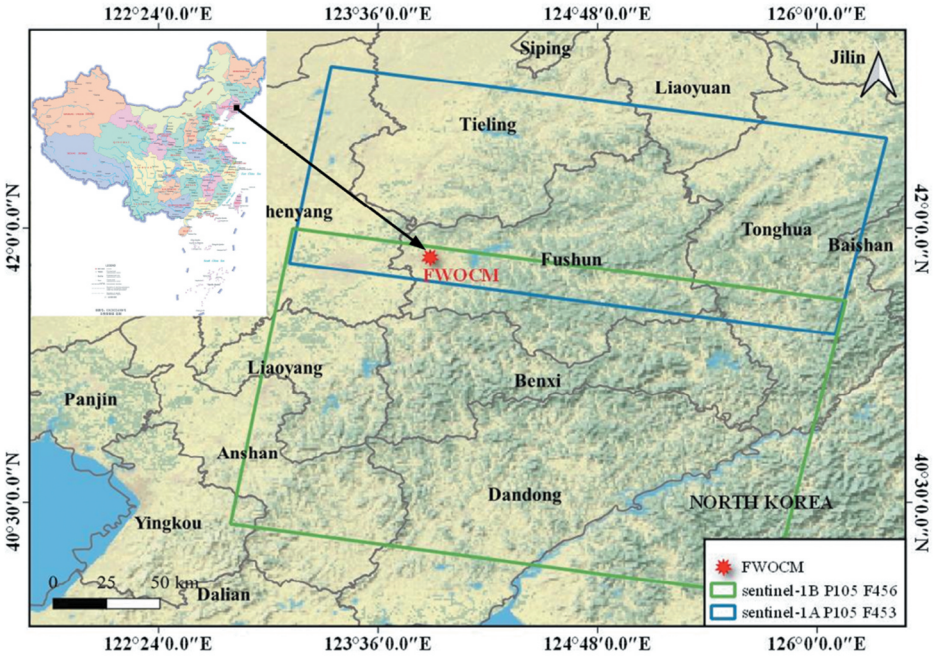

(a) Location of FWOCM and spatial coverage of the processed SAR datasets.

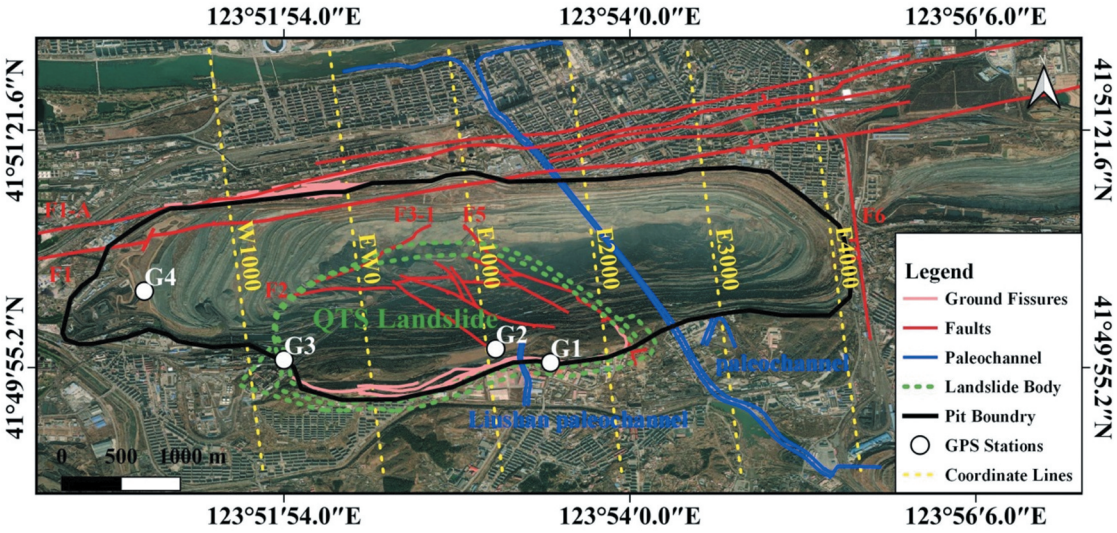

(b) Geological structures in the FWOCM.

Figure 1. The study area of Fushun west opencast coal mine (FWOCM): (a) location of FWOCM and spatial coverage of the SAR datasets; (b) geological structures in the FWOCM.

collected. The Sentinel-1 radar satellite program is a member of the Copernicus satellite mission of the European Space Agency (ESA), which comprises two satellites (Sentinel-1A and Sentinel-1B) with identical C-band SAR sensors onboard. Sentinel-1A was launched in April 2014 and Sentinel-1B was launched in April 2016. The Sentinel-1 satellites adopt a solar-synchronous orbit with a revisit interval of 12 days, and the constellation provides 6 days revisiting time over large part of the earth surface. However, the Sentinel-1B mission ended on 23 December 2021, due to failure of the antenna power supply unit. Therefore, for the FWOCM area, 89 Sentinel-1B descending images acquired during 8 December 2018 to 16 December 2021 prior to the failure are collected (Path 105 Frame 456), whereas 19 Sentinel-1A descending images acquired during 16 March 2022 to 18 October 2022 are collected (Path 105 Frame 453) after the failure of Sentinel-1B, as shown in Figure 1(a). Detailed parameters of the data are shown in Table 1. Unfortunately, there is no acquisition along the ascending orbit covering the investigated area, so we could only analyze the descending orbit avoiding the possibility to compute three dimensional components of the ground motion.

Figure 2. Landslide-induced surface phenomena.

Table 1. The SAR datasets in FWOCM.

Sensor	Number of images	Time period	Orbit Type	Path and Frame	Incidence angle (°)
Sentinel-1B	89	2018/12/08–2021/12/16	Descending	P105 F456	43.81°
Sentinel-1A	19	2022/03/16–2022/10/18	Descending	P105 F453	43.86°

3. Methodology

3.1. Multi-temporal InSAR

Ever since proposal of the classical Permanent Scatterers Interferometric SAR (PS-InSAR) algorithm in 2001, the MT-InSAR technique has been extended to many different algorithms, such as Small BAseline Subsets (SBAS), Stable Point Interferometry over Unurbanized Areas (SPINUA), Coherent Target Analysis (CTA), Spatial-Temporal Unwrapping Network (STUN), Interferometric Point Target Analysis (IPTA), Stanford Method for Persistent Scatterers (StaMPS), Persistent Scatterers Pair (PSP), Quasi Persistent Scatterers (QPS) and SqueeSAR, etc. (Ferretti et al. 2011; Ferretti, Prati, and Rocca 2000, 2001; Hooper 2008; Hooper et al. 2004; Perissin and Wang 2012). The basic idea of these MT-InSAR algorithms is to extract pixels exhibiting coherence over a period and conduct spatial-temporal analysis on the phase time series, for the purpose of accurate displacement estimation. These algorithms differ in the combination strategy of interferometric pairs, point target selection strategy, phase unwrapping algorithm, and whether adopting any deformation models during time series displacement inversion, etc. In this study, the widely adopted SBAS algorithm is used for MT-InSAR analysis.

The SBAS algorithm adopts a multi-master interferometric strategy by making use of all the high-quality differential interferograms with short spatial-temporal baselines. This combination of interferometric pairs can improve the temporal sampling rate of deformation time series and weaken the influence of spatial-temporal decorrelation, which is beneficial to atmospheric phase removal, resulting in more reliable displacement estimations (Orhan 2021). Therefore, it is more suitable for conducting long time series analysis for FWOCM. The key steps involved in SBAS processing are shown in Figure 3. First of all, a reference image is selected according to the total coherence of the spatial-temporal baselines, and all other images are registered with reference to it. Secondly, differential interferograms are generated using the registered SAR images according to given thresholds on the spatial and temporal baselines. Thirdly, the differential interferograms stack is unwrapped with Delaunay minimum cost flow algorithm. Then, the coherent targets are selected based on phase time series analysis, and the interferometric phase time-series are generated by inverting the unwrapped interferograms through the Singular Value Decomposition (SVD) method. The unwrapped phase of each pixel comprises components from target displacement, topographic residuals, atmospheric disturbance, orbital error, and noise. By applying iterative filtering in spatial-temporal domains, these different components could be successfully separated, and the displacement in Line Of Sight (LOS) is finally retrieved (Berardino et al. 2002; Lanari et al. 2004).

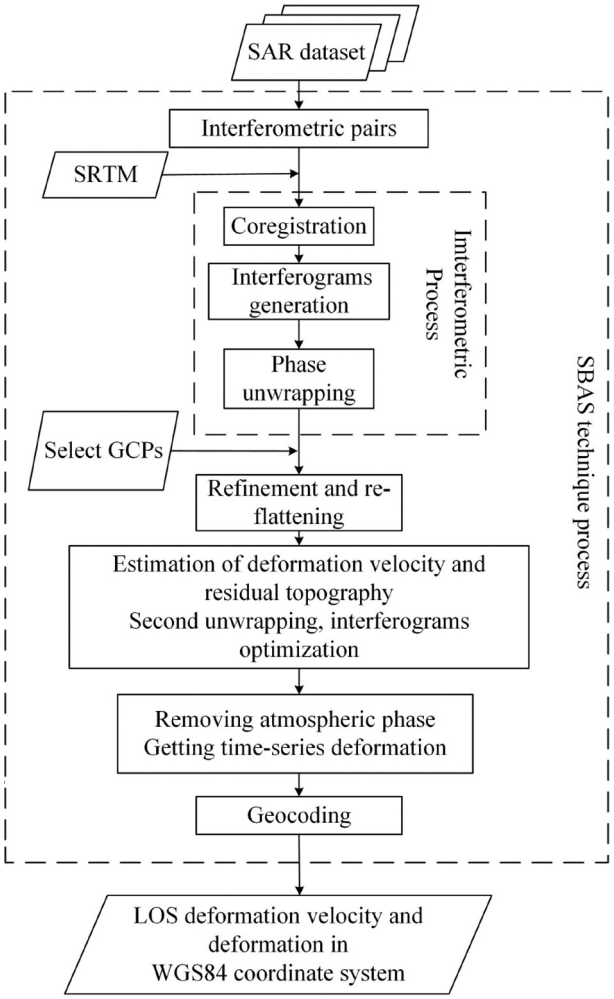

Figure 3. Key steps of SBAS algorithm.

3.2. The cross wavelet transform

In order to quantitatively analyze the response of displacement to precipitation, we adopted the Cross Wavelet Transform (XWT) between the time series displacements and precipitation. Wavelet analysis is a powerful tool for quantifying non-stationary and discontinuous time series, which has been widely adopted in signal processing. It can determine which time domain or frequency domain the vibration of different signals occurs by conducting multi-scale refinement. In wavelet analysis, a signal can be decomposed into a series of wavelets derived from a mother wavelet by translation and scaling. These irregular wavelets are used to approximate the sharp changes in a non-stationary signal and the discrete discontinuous signal with some local characteristics, for more realistic transformation of the original signal into a certain time scale. However, wavelet analysis can only explore the time-frequency variation characteristics of a single time series, and it is difficult to analyze the interaction and time-frequency correlation between multiple time series signals.

Based on the traditional wavelet analysis theory, the XWT is a new multi-signal multi-scale analysis technology which can not only effectively analyze the correlation between two time series, but also reflect the phase structure and detailed characteristics of both signals in the time and frequency domains. The XWT is widely used in many fields, such as geology and hydrology, etc. (Adamowski 2008; Boako and Alagidede 2017; Durocher et al. 2016). For a certain time domain signal $x(t)$, its wavelet transform is defined as follows:

$$W_x(a,\tau) = a^{-1/2}\int_{-\infty}^{+\infty} x(t)\psi^*\left(\frac{t-\tau}{a}\right)dt$$
$$\psi(t) = \pi^{-1/4}\left(e^{-j\omega_0{}^2/2} - e^{-\omega_0{}^2/2}\right)e^{-t^2/2} \quad (1)$$

where, ψ is the mother wavelet; $a(a>0)$ is the scale operator; τ is the displacement operator; $*$ denotes the complex conjugate; ω_0 is the initial phase angle; $\psi(t)$ is the morlet wavelet function commonly used as mother wavelet. For two different time-domain signals $x(t)$ and $y(t)$, the cross wavelet transform between them is defined as:

$$W_{xy}(a,\tau) = W_x(a,\tau)W_y{}^*(a,\tau) \quad (2)$$

Where $\left|W_{xy}(a,\tau)\right|$ is the cross-wavelet Power Spectral Density (PSD) containing time-frequency-amplitude information, which reveals the contribution of the two signal sequences to the overall variance at each harmonic component. Generally, higher cross-wavelet power spectral density indicates stronger correlation between the two signals.

The phase angle of cross-wavelet is used to estimate the phase difference between two different time series, which can be considered as the temporal difference between them. The phase angle of a cross-wavelet is defined as:

$$arctan\left(\frac{i_{mag}\left\{W_{xy}(a,t)\right\}}{r_{eal}\left\{W_{xy}(a,t)\right\}}\right) \quad (3)$$

Where $r_{eal}\left\{W_{xy}(a,\tau)\right\}$ and $i_{mag}\left\{W_{xy}(a,\tau)\right\}$ are the real and imaginary parts of the cross-wavelet respectively. In a cross-wavelet PSD map, when the phase angle arrow points to the time increase direction, it indicates there is a positive correlation between the two time series at the corresponding time scale. On the other hand, when the cross-wavelet correlation coefficient is high, the temporal difference can be estimated by the angle between the wavelet phase arrow and the time axis.

In cross wavelet transform, the correlation between two time series in a certain time-frequency range can be described by the Wavelet Transform Coherence (WTC), which is expressed as follows:

$$R_n^2(s) = \frac{\left|S(s^{-1}W_{xy}(s))\right|^2}{S(s^{-1}\left|W_x(s)\right|^2)\cdot S(s^{-1}\left|W_y(s)\right|^2)} \quad (4)$$

Where $\left|S(s^{-1}W_{xy}(s))\right|^2$ is the cross product of two time series signals at a certain amplitude, $S(s^{-1}|W_x(s)|^2)$ and $S(s^{-1}|W_y(s)|^2)$ are the amplitude of the oscillating wave, and S is the smoothing operator. In this paper, only the bit-phase arrows of the WTC $R_n^2(s) \geq 0.5$ are marked.

In order to evaluate the reliability of the XWT results, statistical tests at certain significance levels need to be performed. In this paper, the cross-wavelet power spectrum is tested against the standard spectrum of red noise, to finally determine the significance of the correlation between precipitation and seasonal displacements. For the two time series signals, when the cross-wavelet power spectrum exceeds the upper boundary of the 95% confidence interval of the red noise power spectrum, it is considered the red noise test at the significance level of $\alpha = 0.05$ is passed, and the correlation between the two is considered significant.

4. Experimental results analysis

4.1. The LOS displacements of FWOCM

The 108 Sentinel-1 SAR images are processed as three different stacks respectively with almost identical parameter settings. During the period from 8 December 2018 to 21 December 2020, 211 differential interferograms out of 60 SAR images were generated for MT-InSAR analysis. During the period from 2 January 2021 to 16 December 2021, 100 differential interferograms out of 29 SAR images were generated for MT-InSAR analysis. During the period from 16 March 2022 to 18 October 2022, 80 differential interferograms out of 19 SAR images were generated for MT-InSAR processing. The spatial-temporal baseline distributions are shown in Figure 4. During MT-InSAR processing, the considered Sentinel-1 data were multi-looked with values of 1 along the azimuth and 4 along the range directions respectively. All the

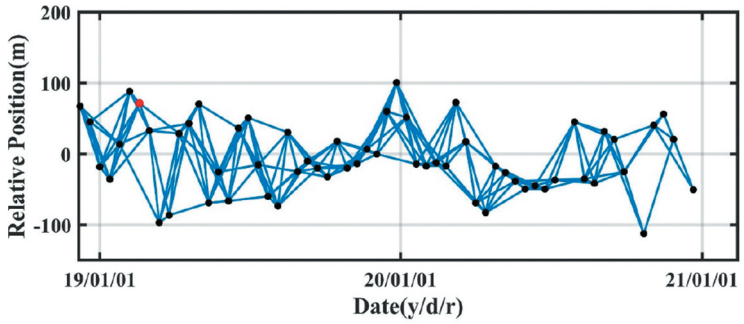

(a) 2018.12.08 - 2020.12.21.

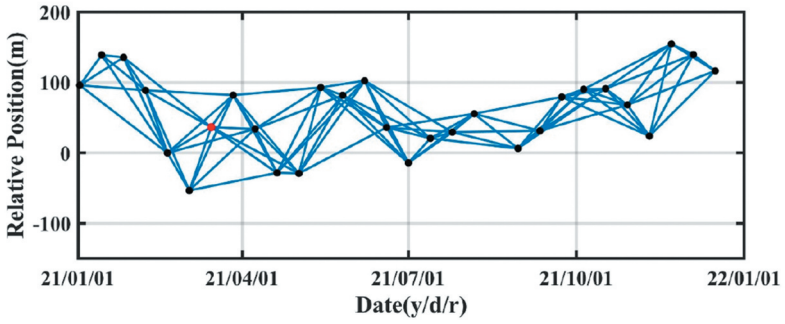

(b) 2021.01.02-2021.12.16.

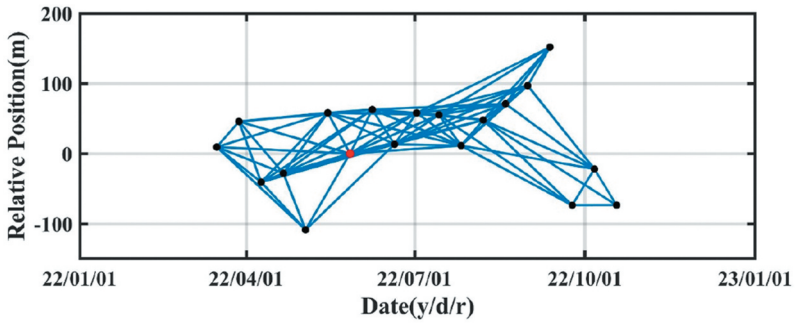

(c) 2022.03.16-2022.10.18.

Figure 4. The spatial-temporal baseline distributions of the during MT-InSAR processing.

differential interferograms were then filtered using the Goldstein filter forming the unwrapped data stacks. The data stacks were successively inverted using the Singular Value Decomposition (SVD) method to obtain the displacement time series and the mean ground velocity maps. At this stage, the atmospheric contribution was estimated and removed via a double filtering in time and space domain. Finally, the results were geocoded to the geographic coordinate system.

The annual LOS displacement velocities of FWOCM derived by MT-InSAR are shown in Figure 5, where the displacement velocities maps of the three different periods are generally similar, although with slight variation at some parts. The displacements of FWOCM are mainly located at five different areas, as shown in Figure 5. Area 1 is the Qian Tai Shan (QTS) landslide area on the south slope (highlighted by green dashed lines), area 2 is located at the northeastern part of the mining pit, area 3 is the

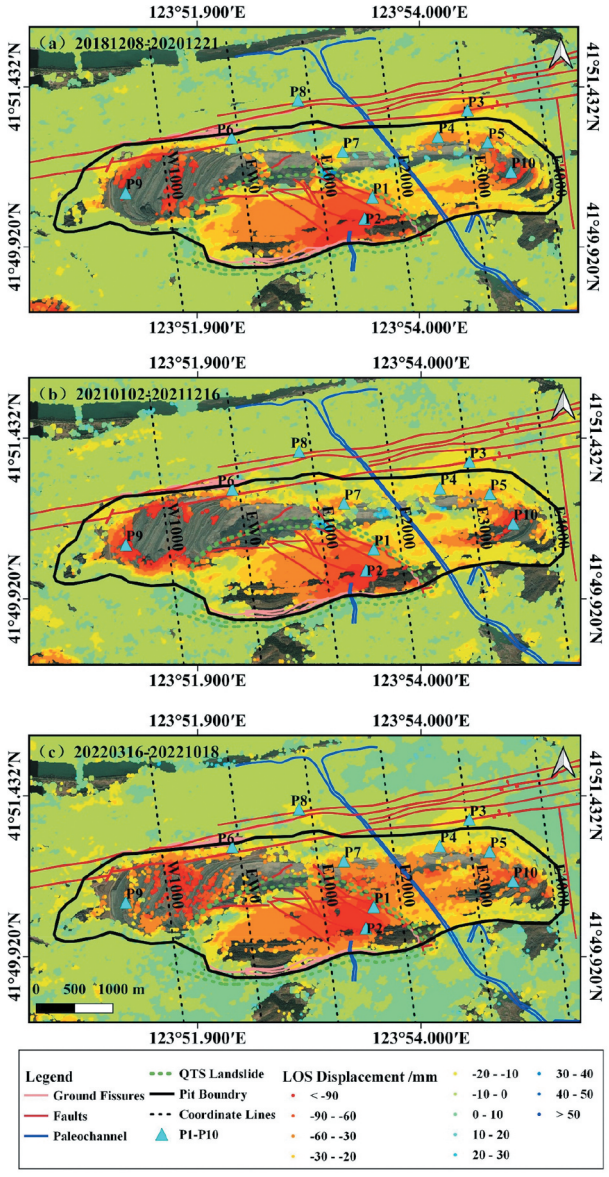

Figure 5. The LOS displacements of FWOCM in three different monitoring periods.

historical landslide area located at the central and western part of the north slope, area 4 is on the west slope and area 5 is on the east slope of the mining pit. Detailed information about the five displacement areas are given in the following parts.

(1) Area 1 - the QTS landslide on the south slope

The QTS landslide is the largest landslide in FWOCM (as shown in Figure 6), of which the sliding speed exceeded 20 m per year from 2013 to 2016 and decelerated after 2017. Spatially, the displacement of the QTS landslide is generally focused on the eastern part (with line E1000 as the boundary), due to the continuous backfilling with mining wastes at the landslide toe. On the other hand, displacement rate of the western part of QTS landslide is much smaller. Interestingly, the area exhibiting the largest displacement rate on the QTS landslide is in vicinity of the Liushan paleochannel. Temporally, the eastern half of QTS landslide experienced a slight decrease in 2021 and slight increase in 2022 with maximum displacement velocity generally identical to 2018–2020. However, by contrast to 2018–2020, the major displacement area has moved downslope as a whole in 2022. Although the overall displacement rate of the western half of QTS landslide is smaller than the eastern half, there is also a trend of decreasing in 2021 and then increasing in 2022, as compared with 2018–2020. It is worth noting that the displacement velocities of the western half of QTS landslide in 2022 are slightly higher than that in 2018–2020.

(2) Area 2 - the northeastern part of the mining pit

In recent years, excavation of oilshale in FWOCM was mainly conducted at the bottom of the northeast part, and stopped in 2020. Affected by the mining activities, in early 2018, an elliptical subsidence area along the fracture zone of fault F1 (centered at the junction of E3000 and fault F1) was formed at the beginning of 2018, as shown in Figure 7. The maximum subsidence rate of this area exceeded 50 mm per year during 2018–2020, and gradually decreased to approximately 25 mm per year till 2022. Since the oilshale excavation has stopped in FWOCM, this subsidence area is expected to gradually stabilize in the future. Due to the influence of mining activities in recent years, there are also some local displacements on the north slope of FWOCM. The displacement rates to the east of E3000 are generally identical during the three monitoring periods, whereas those to the west of E3000 decelerated in 2021 and 2022 by contrast to 2018–2020, due to the reduction of mining activities.

(3) Area 3 - the historical landslide area on the central and western part of the north slope

There have been many large-scale catastrophic landslides happened at the central and western parts of the north slope in FWOCM prior to 2016, and abundant slope treatment has been carried out.

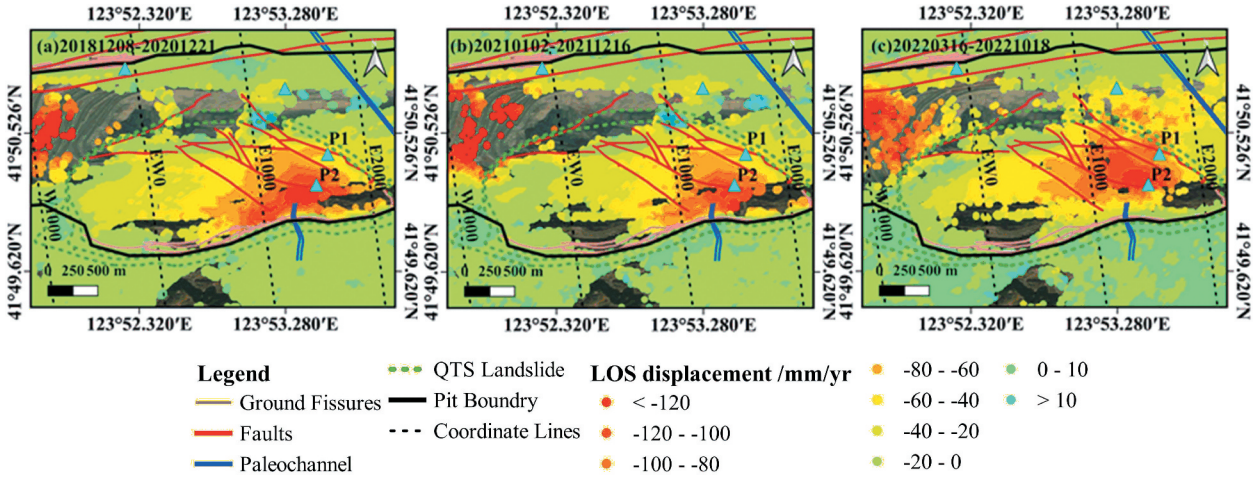

Figure 6. Displacement of the Qian Tai Shan (QTS) landslide.

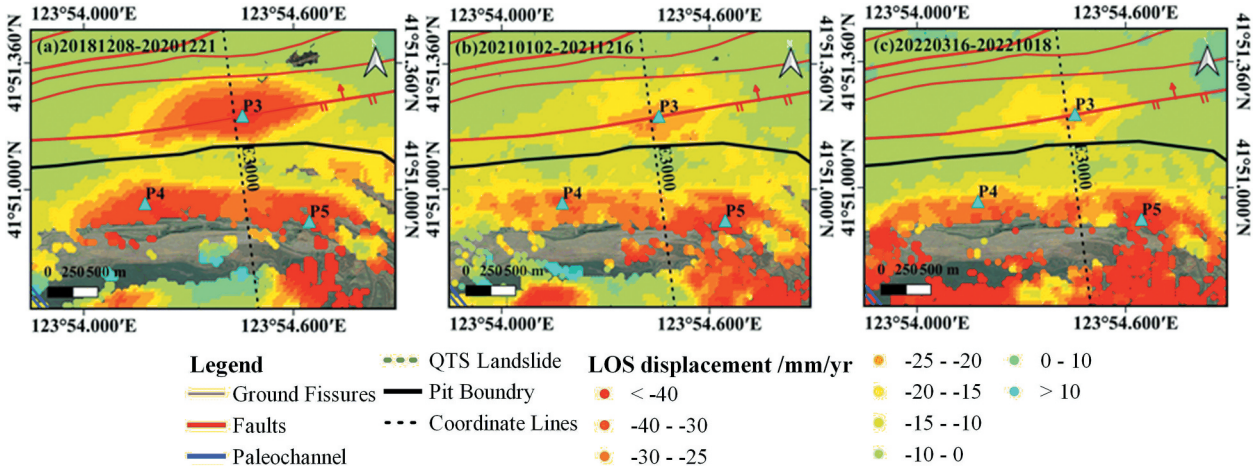

Figure 7. Displacement on the eastern part of the north slope.

After the slope treatments, this historical area was generally stable during 2018–2020, as shown in Figure 8. In 2021, a small-scale displacement area was found in vicinity of EW0, however slowed down in 2022. In 2021, a small subsidence funnel appeared in the former Fushun power plant (in vicinity of the junction of fault F1A and E1000), which continued to increase in 2022 with maximum subsidence rate exceeding 20 mm per year.

(4) Area 4 - the west slope of FWOCM

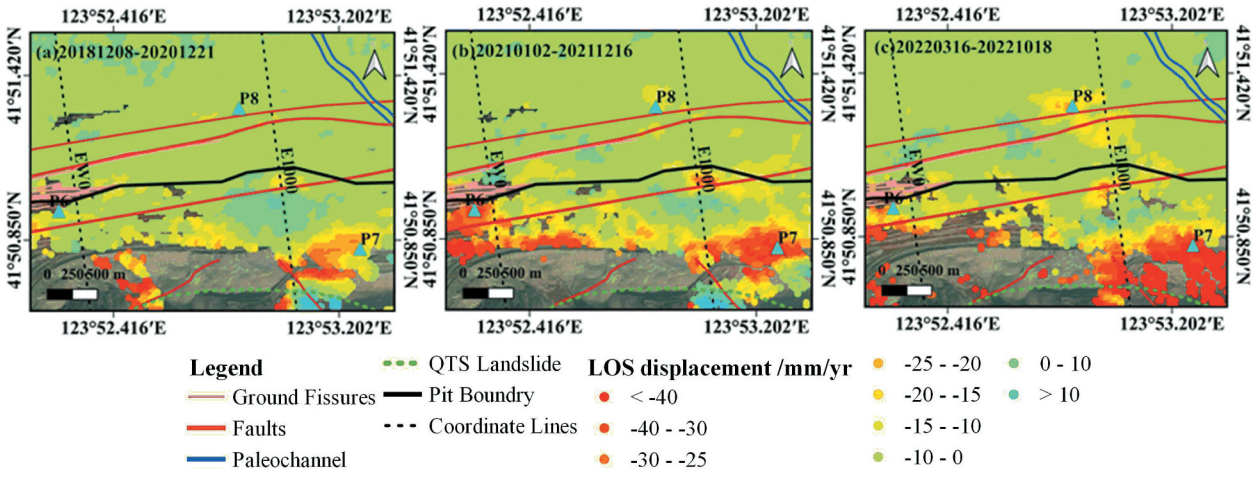

Figure 8. Displacement of the historical landslide area on the central and western part of the north slope.

The west slope of FWOCM has been deforming for a very long time. However, since the west slope has been reclaimed and has very gentle slope angle, the long term displacements are mainly caused by consolidation of the of the backfill materials. This consolidation would gradually stabilize over time, which has little impact on the safety of FWOCM. As shown in Figure 9, the displacement velocities to the west of W1000 hve decreased in 2022, although the area to the east of W1000 still suffers from ground subsidence.

(5) Area 5 - the east slope of FWOCM

The displacement velocities on the east slope of FWOCM were relatively large in 2018–2020 and 2021, and decreased in 2022 except for some small areas, as shown in Figure 10. However, due to the steep slope angle of the east slope and frequent passing of vehicles, displacement of this area is probably a potential threat to the FWOCM.

The time series displacements of ten points (P1-P10 marked in Figure 5) located at different parts of the FWOCM are plotted in Figure 11. Displacement rates of the ten points during the three different monitoring periods are shown in Table 2. The displacement rate of P9 (located on the west slope) was 124.09 mm per year, and decreased to 97.24 mm per year in 2021, and further decreased to 42.33 mm per year in 2022, indicating gradual stabilization of the west slope. Similarly, P4 and P3 also experienced gradual decrease of the displacement rates, indicating stabilization of the eastern part of the north slope. P6 and P5 located on the north slope have all experienced acceleration first and then deceleration during the three monitoring periods, this means stability of the north slope has been reinforced. And, similar temporal characteristics are also found for P10 located on the east slope. Displacement of P7 (located also on the north slope) in 2022 is generally identical to that of 2021, however slightly larger than that of 2018–2020. However, displacement rates of P2 and P1 located at QTS landslide on the south slope both remain higher than the other points, and there is even some slight acceleration on P1 (in vicinity of fault F5) in 2022, which means the QTS landslide

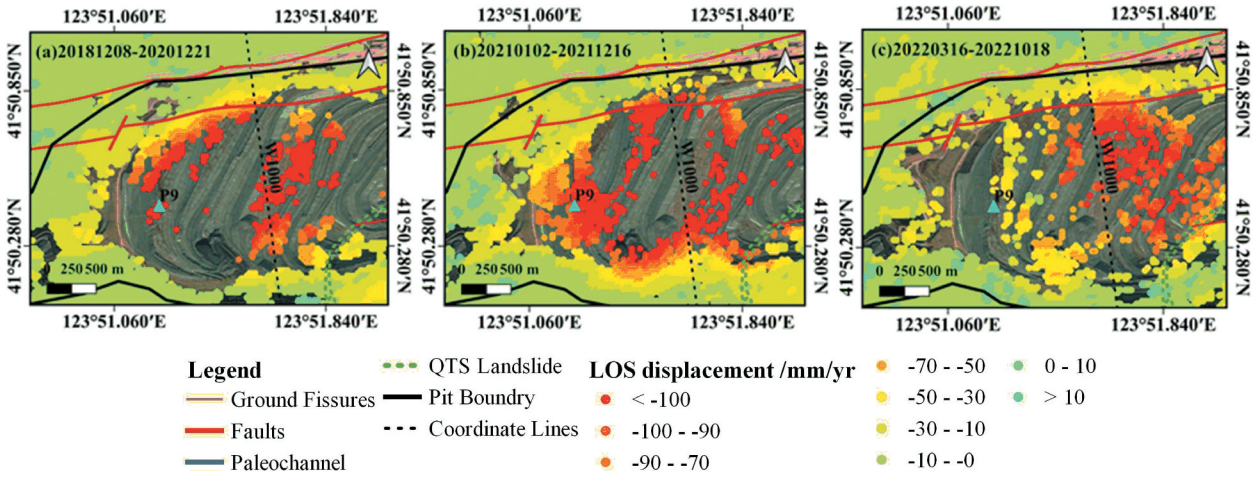

Figure 9. Displacement on the west slope of FWOCM.

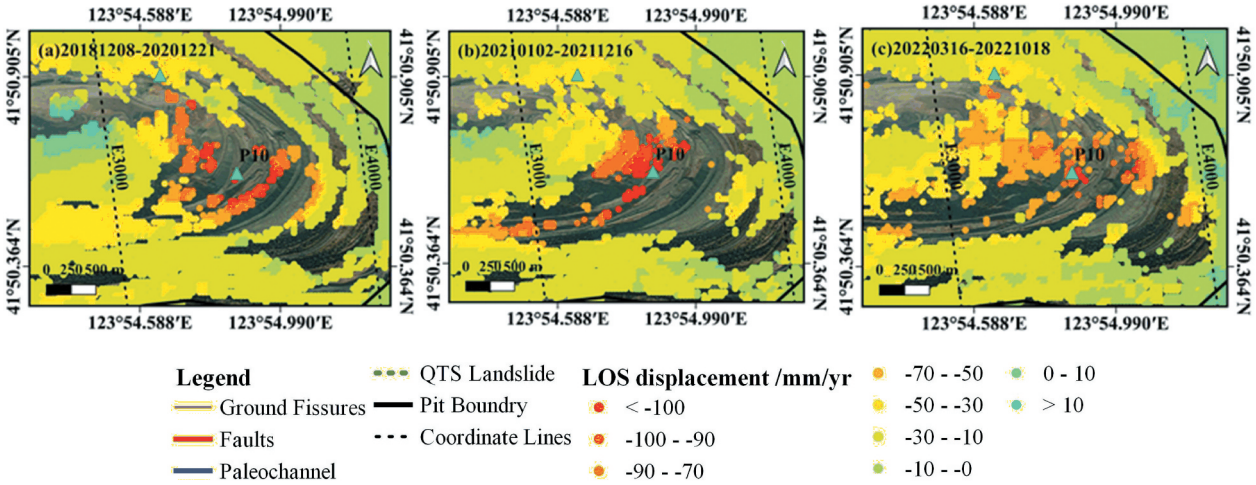

Figure 10. Displacement of the east slope in FWOCM.

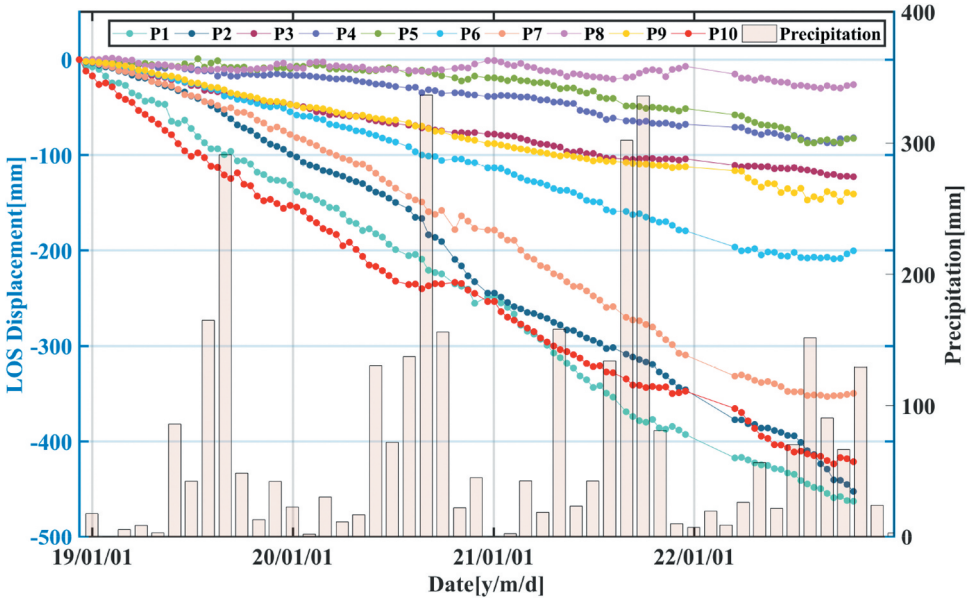

Figure 11. Time series displacements of the 10 points in FWOCM.

Table 2. Displacement velocities of P1-P10 during the three monitoring periods.

ID	Location	2018.12.08～2020.12.21 LOS velocities (mm per year)	2021.01.02～2021.12.16 LOS velocities (mm per year)	2022.03.016～2022.10.18 LOS velocities (mm per year)
P1	QTS landslide	68.45	68.82	85.39
P2	QTS landslide	133.2041 (max)	131.38 (max)	132.15
P3	Fushun city	42.82	25.32	2.85
P4	North slope	41.35	3.44	23.53
P5	North slope	37.82	48.62	45.79
P6	North slope	1.49	41.13	17.13
P7	North slope	21.73	39.49	39.54
P8	Former power plant	1.88	12.29	21.92
P9	West slope	124.09	97.24	42.33
P10	East slope	121.24	155.55	9.85

(especially the east part) is still the most dangerous landslide in FWOCM. It is worth noting that the displacement velocity of P8 (located in the former thermal power plant) has been gradually increasing during the three monitoring periods, which exceeded 20 mm per year in 2022.

Among the 10 points, the linear deformation and seasonal fluctuation of points P2 and P10 are both very clear, especially during 2020–2021. Seasonal fluctuations are also found in the other points, however with much smaller magnitude. This is because most of the other points are located on the north slope and the urban area of Fushun city. Since most of the landslides in history occurred on the north slope of FWOCM, extensive control measures have been taken on the north slope. Therefore, the infiltration of rainwater is limited on the north slope. Similarly, ground surface in the Fushun urban area is mainly composed of impermeable layers (e.g. asphalt or cement), so the precipitation infiltration problem is also limited. Therefore, we conducted cross wavelet transform on P2 and P10 to analyze their deformation response to precipitation.

4.2. Accuracy assessment

In order to assess the accuracy of the MT-InSAR displacements, cross comparison with GNSS measurements is conducted. Since the GNSS measurements are in three dimensional space, whereas the MT-InSAR results are in the LOS direction, they have to be converted to identical dimensions for comparison. Methods on resolving three-dimensional displacements from InSAR measurements have been studied by predecessors (Hu et al. 2014). At least three independent InSAR measurements from different viewing geometry are necessary to retrieve three-dimensional displacement vector (north, east, vertical). Unfortunately, there is only one descending Sentinel-1 stack covering the investigated area, so we are not able to retrieve the accurate three dimensional displacements from the MT-InSAR results. On the other hand, the three dimensional GNSS measurements are projected to the LOS direction for comparative analysis. According to the side-looking SAR geometry, the MT-InSAR displacement (denoted by D_{Los}) is expressed as the projection of a three dimensional deformation vector onto the radar LOS direction, as shown by the following equation:

$$D_{LOS} = D_v \cdot \cos\theta + D_n \sin\alpha \sin\theta - D_e \cdot \cos\alpha \sin\theta \quad (5)$$

Where D_e is the deformation in east-west direction; D_n is the deformation in north-south direction; D_v is the deformation in vertical direction; α is the satellite heading angle (clockwise from the north), and θ is the radar incidence angle (Hu et al. 2014; Li et al. 2023). To guarantee the accuracy of this conversion, instead of using one unique incidence angle for all pixels, independent incidence angles for different pixels are calculated according to their coordinates in the SAR image. Limited to the temporal coverage of GNSS measurements, cross comparison is only conducted for the year 2021. The time series displacements of the four points (G1-G4) marked in Figure 1(b) are depicted in Figure 12, where the GNSS time series displacements fluctuate significantly due to the low accuracy in vertical direction. Despite of the fluctuation of GNSS measurements, time series displacements estimated by MT-InSAR shows an obvious linear trend, and in very good agreement with the GNSS measurements.

5. Discussion on the displacement influence factors

5.1. Engineering geology

The engineering geological conditions of the FWOCM are very complicated, with many faults developed, which influence the stability of the mining pit. Among the five major displacement areas, the QTS landslide is strongly influenced by the geological conditions, especially by the E-W trending fault F2, the NW-SE trending fault F5 and multiple associated faults of F5 developed on the QTS landslide body. Fault F2 strikes nearly in E-W direction and is located at the north of the QTS landslide body. There is a rockfall area in coordinates W1200~E300 on the upper part of fault F2, where landslides and rock falling have occurred for many times. Fault F3–1 is located at the northwest boundary of the QTS landslide, whereas fault F5 is located at the east boundary. Fault F5 is a tensional and torsional normal fault with strike in NW-SE. The lithology of the QTS landslide is tuff with basalt, and there is a 50 m wide fracture zone in vicinity of F5. Besides, several faults associated to F5 are also located at the edge of the QTS landslide and threatening its stability.

According to engineering geology, the QTS landslide in FWOCM is initiated by instability of the upper part of the landslide body, and followed by shearing of the slope toe, which belongs to a high slope bedding rock landslide with pushing slip. On the south slope, the basalt of Laohutai Formation is the floor of the coal seam, with Archean granite gneiss underlying, as shown in Figure 13. It is inferred that the contact

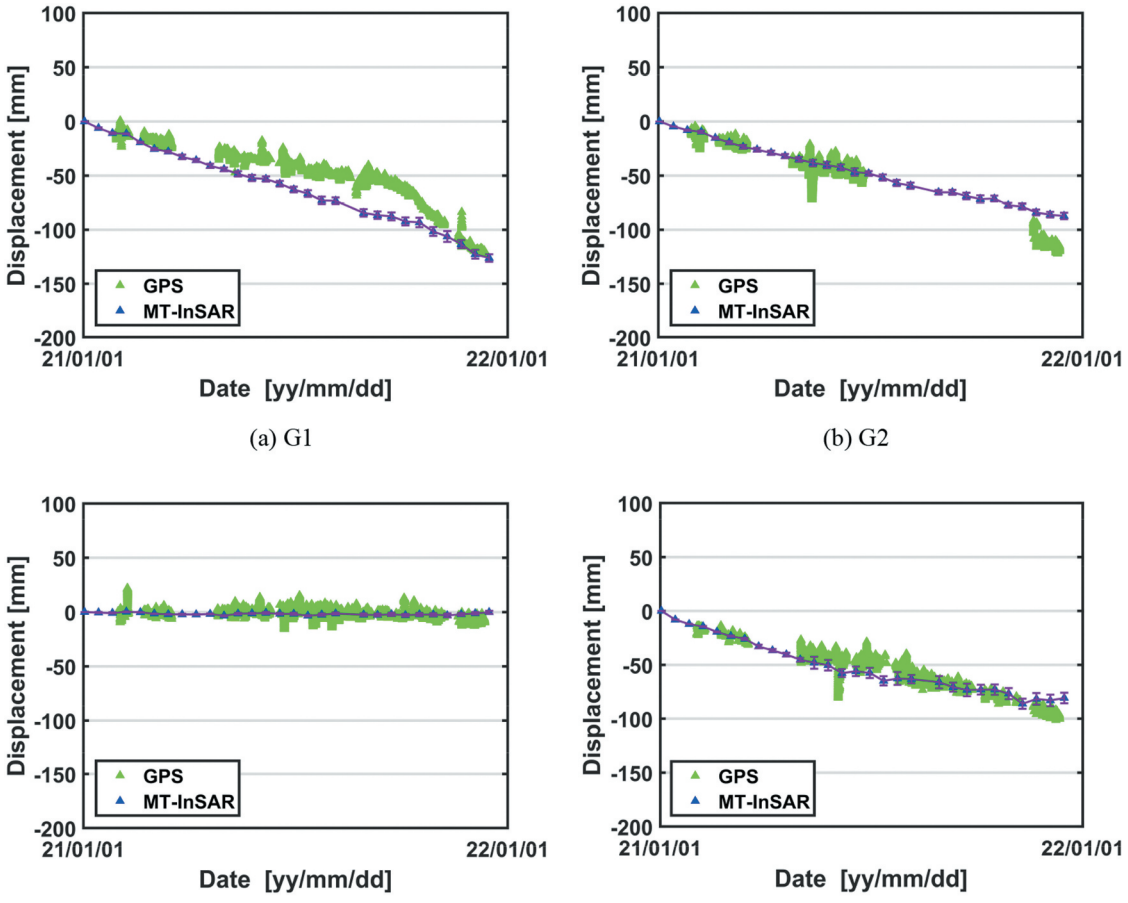

Figure 12. Cross comparison with GNSS measurements (G1-G4).

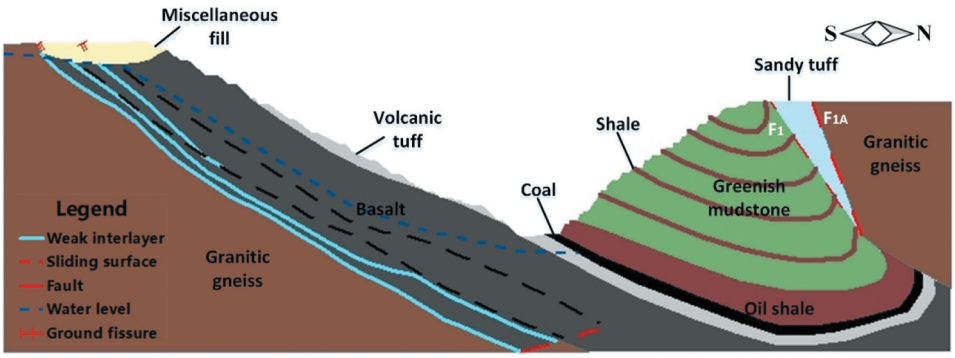

Figure 13. The rock stratum of FWOCM.

surface of the two rock layers and the weak interlayers in the basalt are the sliding surfaces of QTS landslide. There are many weak intercalations in the basalt volcanic rock, which are controlled by the weak intercalations between the multiple layers. During mining process, slope instability gradually occurs under the combined influence of blasting, increase of slope angles and water infiltration, and these weak intercalated layers become the sliding surfaces of QTS landslide.

Stability of the QTS landslide is also influenced by the slope inclination, the relationship between the rock strata and joints of the south slope in FWOCM. The geological structure of FWOCM is a syncline structure, and the south slope gradually becomes a bedding slope after coal mining. Secondly, basalt is exposed in a large area on the south slope, and the structural plane is mostly inclined to the north, with an inclination of approximately 30°, very close to the inclination of the southern slope. In addition, the joint fissures of the rock mass of the southern slope are very developed, and the rock mass structure is blocky and fractured. In addition, the joint fissures are mainly tensile fissures with strike of NE and NW, which is basically consistent with the direction of the fault structure in the mining area. The consistency of these trends is not conducive to the stability of the south slope.

5.2. Precipitation and groundwater

Displacement of the eastern part of QTS landslide is larger than the western part, especially in the area close to the Liushan paleochannel with undercutting bedrock. The pebble layer of the paleochannel has good permeability, resulting in easy penetration of the precipitation and surface water into the bedrock cracks of the slope, which is not conducive to the stability of the slope. As shown by the displacement time series, the displacement velocities accelerate annually during the rainy season from July to September. When there is limited amount of precipitation, the groundwater in the slopes remains balanced, and the slopes remain stable due to the unchanged stress field.

It is noteworthy that P2 and P10 exhibit opposite seasonal deformation characteristics (as shown in Figure 14(a) in the revised manuscript), which are probably associated to their respective geological conditions. P2 is located near the Liushan paleochannel on QTS landslide, where the largest deformation is detected. This area is well-developed with faults, and there is a river pebble layer near Liushan paleochannel. These faults and pebble layers provide infiltration channels for rainwater, and will form weak interlayers. Therefore, the water permeability in this area is very strong. The infiltration of rainwater is more likely to increase the saturation and pore pressure of the landslide body, reducing the shear strength of the slope. Therefore, the time series displacement of P2 shows significant acceleration after heavy precipitation. P10 point is located at the bottom of the eastern slope in FWOCM. This area is currently used as a waste dump, where loose piles of mining waste are dumped. Precipitation will increase the water content of the waste dump, which is beneficial for strengthening the support of the loose layer. Therefore, the time series deformation of P10 shows significant deceleration after heavy precipitation.

In order to quantitatively analyze the displacement response to precipitation, cross-wavelet correlation analysis is conducted for P2 and P10. As shown in Figures 14 (b–e), the area which passes red noise test at significance level of 95% is marked by black circles in both the WTC map and XWT map. The black arrows reflect the phase relationship of the two time series involved in cross-wavelet transform. When the arrows point to right, it indicates the two phases are the same and a positive correlation between the two time series is detected, and vice versa. When the arrows point downward, it indicates 1/4 cycle of precipitation changes prior to displacements (corresponding to 3 months), and vice versa. In order to avoid boundary effects and spurious high-frequency wavelet information, only the results inside the the wavelet influence cone (highlighted by the arc lines in the figures) is considered.

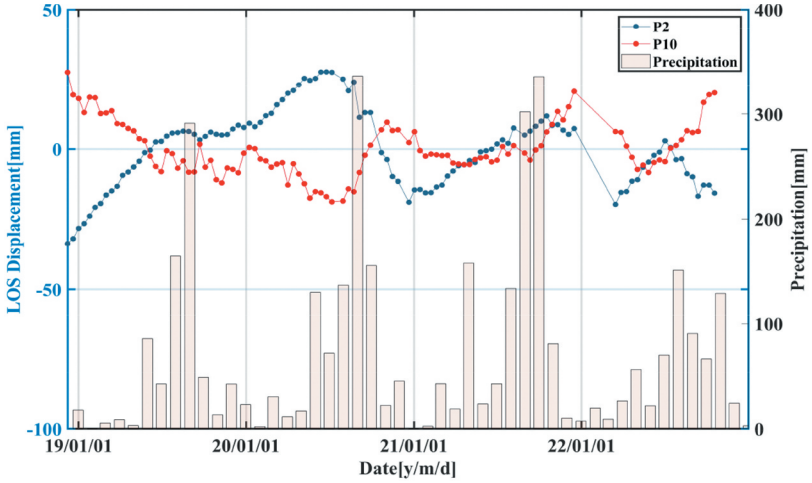

(a) Seasonal displacement time series of P2 and P10.

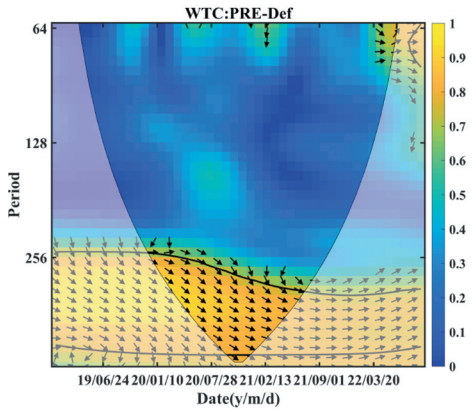

(b) WTC map of P2.

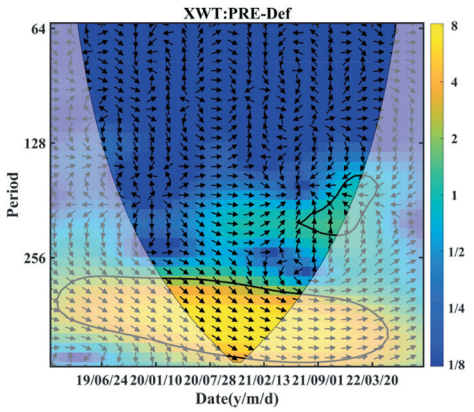

(c) XWT map of P2.

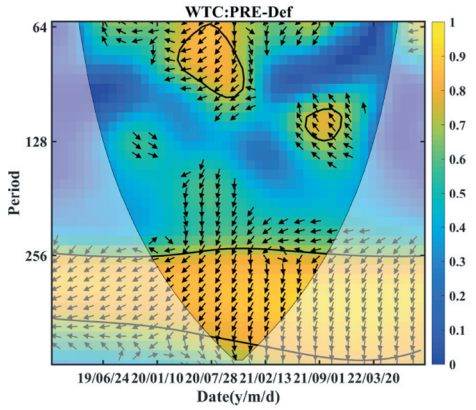

(d) WTC map of P10.

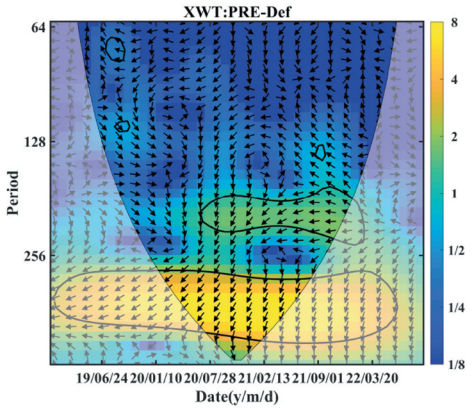

(e) XWT map of P10.

Figure 14. Wavelet spectra between the time series displacements and precipitation for P2 and P10.

As shown in Figure 14(a), precipitation in this study area is mainly concentrated in July and August each year, with accumulative precipitation up to 336 mm in August 2020. After the heavy precipitation in July and August each year, significant displacement changes are found for both P2 and P10. According to the WTC maps shown in Figure 14(b, d), a coherence higher than 0.8 is detected between the displacement and precipitation for both points. As shown in Figure 14(c), there is clearly a positive correlation between the displacement of P2 and precipitation, with a resonance high energy region that passes the 95% confidence test during 30 January 2020 to 24 July 2020. The XWT map in Figure 14(e) shows that a negative correlation is detected between the displacement of P10 and precipitation, with a resonance high energy region that passes the 95% confidence test during 10 January 2020 to 1 September 2021. The black arrows in Figures 14(b–e) all point downward, indicating displacement changes occur after precipitation

change. The phase lag between displacements and precipitation is approximately 30°~45°, indicating that displacements respond to precipitation after approximately 30 ~ 45 days.

6. Concluding remarks

In this paper, the Multi-Temporal Interferometric Synthetic Aperture Radar (MT-InSAR) technology in combination with cross-wavelet analysis is adopted to analyze the displacements of Fushun West Opencast Coal Mine (FWOCM) with Sentinel-1 SAR images acquired from 2018 to 2022. The MT-InSAR results show that displacements of FWOCM are mainly distributed in five areas due to different causative factors. Among the major displacement areas, the Qian Tai Shan (QTS) landslide on the south slope presents seasonal deceleration and acceleration associated to precipitation, with the maximum displacement in vicinity of the Liushan paleochannel. The results of this paper have fully taken in account the complicated characteristics of surface displacements in opencast mining area. By combining MT-InSAR with engineering geological information and other data (e.g. precipitation), it is possible to comprehensively interpret the long-term displacement mechanism of opencast mines, which is of great significance for geological disaster prevention in the investigated mining area.

Disclosure statement

No potential conflict of interest was reported by the author(s).

Funding

This work is supported by the Natural Science Foundation of China [grant number 42071453], the geological hazard investigation project of Liaoning Province [grant number 2022020700179] and the Fund of National Key Laboratory of Science and Technology on Remote Sensing Information and imagery Analysis, Beijing Research Institute of Uranium Geology [grant number 6142A01210407].

Notes on contributors

Lianhuan Wei is an associate professor in the School of Resources and Civil Engineering, Northeastern University. She did her research from Technical University of Munich as a visiting young scientist under the support of China Scholarship Council in 2012 and 2013, and received her PhD in Photogrammetry and Remote Sensing from Wuhan University in 2015. Her research interests include radar remote sensing, geohazard monitoring and susceptibility assessment.

Fang Wang received the B.S. degree in Survey and Mapping Engineering from the Inner Mongolia University of Science and Technology in 2021. She is currently a graduate student at Northeastern University. Her research interest is long-term deformation monitoring of landslides with multi-source SAR data.

Cristiano Tolomei is a researcher at Istituto Nazionale di Geofisica e Vulcanologia. He received the B.S. degree in Remote Sensing Engineering from Università degli Studi Roma "La Sapienza" in 1999. His research interests include radar remote sensing, SAR interferometry, remote sensing data inversion and GIS.

Shanjun Liu is a professor in the School of Resources and Civil Engineering, Northeastern University, and director of the Institute for Geo-informatics and Digital Mine Research. Prof. Liu received the PhD in Geomatics from China University of Mining and Technology (Beijing) in 2003. His research interests include hazard detection and disaster remote sensing.

Christian Bignami is a senior researcher and head of the Remote Sensing Unit of Istituto Nazionale di Geofisica e Vulcanologia. He received the PhD in Electromagnetism from Sapienza University of Roma in 2008. His research interests include analysis of remote sensing data from SAR and optical sensors for geophysical applications.

Bing Li is an engineer at the Tenth Geological Brigade of Liaoning Province. He received the B.S. degree in Geology from Lanzhou University in 2015. His research interests include geological hazard investigation and environmental geology survey.

Donglin Lv is an associate researcher in the Energy Geology Institute, Liaoning Geology and Mineral Resources Group, and a member of China Geological Society. He received the M.S. degree in Geotechnical Engineering from Jilin University in 2016. His research interests include geological disasters investigation, environmental geology investigation and mineral geology.

Elisa Trasatti is a researcher at Istituto Nazionale di Geofisica e Vulcanologia, Rome. She received the PhD in Geophysics from University of Bologna Alma Mater Studiorum, Bologna, in 2004. Her research interests mainly involve geodetic data interpretation and modeling by means of analytical and numerical techniques.

Yuan Cui is an associate researcher at the Tenth Geological Brigade of Liaoning Province. He received the M.S. degree in Geological Engineering from Jilin University in 2018. His main research interests are geological hazard investigation and environmental geology survey.

Guido Ventura is a senior researcher at the Istituto Nazionale di Geofisica e Vulcanologia, and dean of the Faculty of Earth and Environmental Sciences and Chief of Engineering Geology. He received his PhD in Tectonics and Structural Geology from the consortium of the Universities of Camerino, Catania, Cosenza, and Florence in 1995. His research interests include seismic and volcanological activities monitoring and oceanographic campaigns.

Meng Ao is a lecturer in the School of Resources and Civil Engineering, Northeastern University. He received the Ph.D in Photogrammetry and Remote Sensing from Wuhan University in 2020. His research interests include time series InSAR and its applications in geohazard monitoring.

Stefano Salvi is a technological director at the National Earthquake Center of the Istituto Nazionale di Geofisica e Vulcanologia, Roma, Italy. He received the M.Sc. degree in Geology from the University of Roma La Sapienza. His

research interests include natural hazards monitoring and ground displacement assessment with remote sensing data.

Shiliu Wang received the B.S. degree in Survey and Mapping Engineering from Hefei University of Technology in 2023. He is currently a graduate student at Northeastern University. His research interest is landslides monitoring with time series SAR data.

Xingyu Pan received the B.S. degree in Survey and Mapping Engineering from Northeastern University in 2023. She is currently the graduate student at Northeastern University. Her main research interest is time series InSAR technology and geophysical modeling with multi-source data.

ORCID

Lianhuan Wei http://orcid.org/0000-0002-7166-538X
Cristiano Tolomei http://orcid.org/0000-0001-7378-0712
Christian Bignami http://orcid.org/0000-0002-8632-9979
Elisa Trasatti http://orcid.org/0000-0002-2983-045X
Guido Ventura http://orcid.org/0000-0001-9388-9985
Meng Ao http://orcid.org/0000-0001-8609-8202
Stefano Salvi http://orcid.org/0000-0002-7776-6544

Data availability statement

Data that support the results and analyses presented in this paper are freely available online or can be accessed through ad hoc data license agreements. In particular: Sentinel-1 data are available via Copernicus Open Access Hub (https://scihub.copernicus.eu/dhus); the SRTM DEM can be download from NASA's data catalogs (https://search.earthdata.nasa.gov/search); the precipitation data can be downloaded from the China Meteorological Data Center (http://data.cma.cn/). The GNSS data is provided by third party who do not agree on sharing their data publicly.

References

Adamowski, J. F. 2008. "River Flow Forecasting Using Wavelet and Cross-Wavelet Transform Models." *Hydrological Processes* 22 (25): 4877–4891. https://doi.org/10.1002/hyp.7107.

Asif, M., C. Bak, M. W. Saleem, and W. S. Kim. 2015. "Performance Evaluation of Integrated Gasification Combined Cycle (Igcc) Utilizing a Blended Solution of Ammonia and 2-Amino-2-Methyl-1-Propanol (Amp) for Co2 Capture." *Fuel* 160: 513–524. https://doi.org/10.1016/j.fuel.2015.08.008 .

Berardino, P., G. Fornaro, R. Lanari, and E. Sansosti. 2002. "A New Algorithm for Surface Deformation Monitoring Based on Small Baseline Differential SAR Interferograms." *IEEE Transactions on Geoscience and Remote Sensing* 40 (11): 2375–2383. https://doi.org/10.1109/TGRS.2002.803792.

Boako, G., and P. Alagidede. 2017. "Co-Movement of Africa's Equity Markets: Regional and Global Analysis in the Frequency–Time Domains." *Physica A: Statistical Mechanics and Its Applications* 468: 359–380. https://doi.org/10.1016/j.physa.2016.10.088.

Chaulya, S. K., and G. M. Prasad. 2016. "Chapter 1 - Slope Failure Mechanism and Monitoring Techniques." In *Sensing and Monitoring Technologies for Mines and Hazardous Areas*, edited by S. K. Chaulya and G. M. Prasad, 1–86.

Dash, A. K. 2019. "Analysis of Accidents Due to Slope Failure in Indian Opencast Coal Mines." *Current Science* 117 (2): 304–304. https://doi.org/10.18520/cs/v117/i2/304-308.

Dong, J., M. Liao, Q. Xu, L. Zhang, M. Tang, and J. Gong. 2018. "Detection and Displacement Characterization of Landslides Using Multi-Temporal Satellite SAR Interferometry: A Case Study of Danba County in the Dadu River Basin." *Engineering Geology* 240: 95–109. https://doi.org/10.1016/j.enggeo.2018.04.015.

Durocher, M., T. S. Lee, T. B. M. J. Ouarda, and F. Chebana. 2016. "Hybrid Signal Detection Approach for Hydro-Meteorological Variables Combining Emd and Cross-Wavelet Analysis." *International Journal of Climatology* 36 (4): 1600–1613. https://doi.org/10.1002/joc.4444.

Feng, Y., J. Wang, Z. Bai, and L. Reading. 2019. "Effects of Surface Coal Mining and Land Reclamation on Soil Properties: A Review." *Earth-Science Reviews* 191:12–25. https://doi.org/10.1016/j.earscirev.2019.02.015.

Ferretti, A., A. Fumagalli, F. Novali, C. Prati, F. Rocca, and A. Rucci. 2011. "A New Algorithm for Processing Interferometric Data-Stacks: SqueeSAR." *IEEE Transactions on Geoscience and Remote Sensing* 49 (9): 3460–3470. https://doi.org/10.1109/TGRS.2011.2124465.

Ferretti, A., C. Prati, and F. Rocca. 2000. "Nonlinear Subsidence Rate Estimation Using Permanent Scatterers in Differential SAR Interferometry." *IEEE Transactions on Geoscience and Remote Sensing* 38 (5): 2202–2212. https://doi.org/10.1109/36.868878.

Ferretti, A., C. Prati, and F. Rocca. 2001. "Permanent Scatterers in SAR Interferometry." *IEEE Transactions on Geoscience and Remote Sensing* 39 (1): 8–20. https://doi.org/10.1109/36.898661.

He, L., L. Wu, S. Liu, Z. Wang, C. Su, and S. Liu. 2015. "Mapping Two-Dimensional Deformation Field Time-Series of Large Slope by Coupling Dinsar-SBAS with MAI-SBAS." *Remote Sensing* 7 (9): 12440–12458. https://doi.org/10.3390/rs70912440.

Hooper, A. 2008. "A Multi-Temporal InSAR Method Incorporating both Persistent Scatterer and Small Baseline Approaches." *Geophysical Research Letters* 35 (16): L16302–L16302. https://doi.org/10.1029/2008GL034654.

Hooper, A., P. Segall, and H. Zebker. 2007. "Persistent Scatterer Interferometric Synthetic Aperture Radar for Crustal Deformation Analysis, with Application to Volcán Alcedo, Galápagos." *Journal of Geophysical Research* 112 (B7): B07407–B07407. https://doi.org/10.1029/2006JB004763.

Hooper, A., H. Zebker, P. Segall, and B. Kampes. 2004. "A New Method for Measuring Deformation on Volcanoes and Other Natural Terrains Using InSAR Persistent Scatterers." *Geophysical Research Letters* 31 (23). https://doi.org/10.1029/2004GL021737.

Hu, J., Z. Li, X. Ding, J. Zhu, L. Zhang, and Q. Sun. 2014. "Resolving Three-Dimensional Surface Displacements from InSAR Measurements: A Review." *Earth-Science Reviews* 133:1–17. https://doi.org/10.1016/j.earscirev.2014.02.005.

Lanari, R., O. Mora, M. Manunta, J. J. Mallorqui, P. Berardino, and E. Sansosti. 2004. "A Small-Baseline Approach for Investigating Deformations on Full-Resolution Differential SAR Interferograms." *IEEE*

Transactions on Geoscience and Remote Sensing 42 (7): 1377–1386. https://doi.org/10.1109/TGRS.2004.828196.

Li, M., L. Zhang, M. Yang, and M. Liao. 2023. "Complex Surface Displacements of the Nanyu Landslide in Zhouqu, China Revealed by Multi-Platform InSAR Observations." *Engineering Geology* 317:107069–107069. https://doi.org/10.1016/j.enggeo.2023.107069 .

Li, Z., J. Wang, L. Li, L. Wang, and R. Y. Liang. 2015. "A Case Study Integrating Numerical Simulation and GB-InSAR Monitoring to Analyze Flexural Toppling of an Anti-Dip Slope in Fushun Open Pit." *Engineering Geology* 197:20–32. https://doi.org/10.1016/j.enggeo.2015.08.012.

Liu, F., K. Yang, T. Yang, Y. Gao, J. Li, Q. Liu, and Q. Fu. 2022. "Pumped Storage Hydropower in an Abandoned Open-Pit Coal Mine: Slope Stability Analysis Under Different Water Levels." *Frontiers in Earth Science* 10. https://doi.org/10.3389/feart.2022.941119.

Loupasakis, C., V. Angelitsa, D. Rozos, and N. Spanou. 2014. "Mining Geohazards—Land Subsidence Caused by the Dewatering of Opencast Coal Mines: The Case Study of the Amyntaio Coal Mine, Florina, Greece." *Natural Hazards* 70 (1): 675–691. https://doi.org/10.1007/s11069-013-0837-1 .

Mora, O., J. J. Mallorqui, and A. Broquetas. 2003. "Linear and Nonlinear Terrain Deformation Maps from a Reduced Set of Interferometric SAR Images." *IEEE Transactions on Geoscience and Remote Sensing* 41 (10): 2243–2253. https://doi.org/10.1109/TGRS.2003.814657.

Mu, Z., J. Yang, G. Liu, Y. Zhang, and J. Jiao. 2022. "Investigation on Mechanism of Coal Burst Induced by the Geological Weak Surface Slip in Coal Seam Bifurcation Area: A Case Study in Zhaolou Coal Mine, China." *Lithosphere* 2022 (Special 11). https://doi.org/10.2113/2022/6780739.

Nguyen, L. C., P. V. Tien, and T. N. Do. 2020. "Deep-Seated Rainfall-Induced Landslides on a New Expressway: A Case Study in Vietnam." *Landslides* 17 (2): 395–407. https://doi.org/10.1007/s10346-019-01293-6.

Nie, L., Z. Li, Y. Lv, and H. Wang. 2017. "A New Prediction Model for Rock Slope Failure Time: A Case Study in West Open-Pit Mine, Fushun, China." *Bulletin of Engineering Geology and the Environment* 76 (3): 975–988. https://doi.org/10.1007/s10064-016-0900-8.

Nie, L., Z. Li, M. Zhang, and L. Xu. 2015. "Deformation Characteristics and Mechanism of the Landslide in West Open-Pit Mine, Fushun, China." *Arabian Journal of Geosciences* 8 (7): 4457–4468. https://doi.org/10.1007/s12517-014-1560-2 .

Onder, S., and M. Mutlu. 2017. "Analyses of Non-Fatal Accidents in an Opencast Mine by Logistic Regression Model – a Case Study." *International Journal of Injury Control and Safety Promotion* 24 (3): 328–337. https://doi.org/10.1080/17457300.2016.1178299.

Orellana, F., J. Hormazábal, G. Montalva, and M. Moreno. 2022. "Measuring Coastal Subsidence After Recent Earthquakes in Chile Central Using SAR Interferometry and GNSS Data." *Remote Sensing* 14 (7): 1611–1611. https://doi.org/10.3390/rs14071611 .

Orhan, O. 2021. "Monitoring of Land Subsidence Due to Excessive Groundwater Extraction Using Small Baseline Subset Technique in Konya, Turkey." *Environmental Monitoring and Assessment* 193 (4). https://doi.org/10.1007/s10661-021-08962-x.

Orhan, O., T. Oliver-Cabrera, S. Wdowinski, S. Yalvac, and M. Yakar. 2021. "Land Subsidence and Its Relations with Sinkhole Activity in Karapınar Region, Turkey: A Multi-Sensor InSAR Time Series Study." *Sensors (Switzerland)* 21 (3): 1–17. https://doi.org/10.3390/s21030774.

Osmanoğlu, B., F. Sunar, S. Wdowinski, and E. Cabral-Cano. 2016. "Time Series Analysis of InSAR Data: Methods and Trends." *ISPRS Journal of Photogrammetry and Remote Sensing* 115: 90–102. https://doi.org/10.1016/j.isprsjprs.2015.10.003.

Ouyang, C., W. Zhao, Q. Xu, D. Peng, W. Li, D. Wang, S. Zhou, and S. Hou. 2018. "Failure Mechanisms and Characteristics of the 2016 Catastrophic Rockslide at Su Village, Lishui, China." *Landslides* 15 (7): 1391–1400. https://doi.org/10.1007/s10346-018-0985-1.

Papageorgiou, E., M. Foumelis, E. Trasatti, G. Ventura, D. Raucoules, and A. Mouratidis. 2019. "Multi-Sensor SAR Geodetic Imaging and Modelling of Santorini Volcano Post-Unrest Response." *Remote Sensing* 11 (3): 259–259. https://doi.org/10.3390/rs11030259.

Park, J., Y. Lee, M. Jin, S. Park, D. Lee, J. Bae, J. Kim, K. Song, and Y. Choi. 2017. "Enhancement of Slurryability and Heating Value of Coal Water Slurry (CWS) by Torrefaction Treatment of Low Rank Coal (LRC)." *Fuel* 203:607–617. https://doi.org/10.1016/j.fuel.2017.03.016.

Perissin, D., and T. Wang. 2012. "Repeat-Pass SAR Interferometry with Partially Coherent Targets." *IEEE Transactions on Geoscience and Remote Sensing* 50 (1): 271–280. https://doi.org/10.1109/TGRS.2011.2160644.

Rosen, P. A., S. Hensley, I. R. Joughin, F. K. Li, S. N. Madsen, E. Rodriguez, and R. M. Goldstein. 2000. "Synthetic Aperture Radar Interferometry." *Proceedings of the IEEE* 88 (3): 333–382. https://doi.org/10.1109/5.838084.

Samsonov, S., N. d'Oreye, and B. Smets. 2013. "Ground Deformation Associated with Post-Mining Activity at the French–German Border Revealed by Novel InSAR Time Series Method." *International Journal of Applied Earth Observation and Geoinformation* 23: 142–154. https://doi.org/10.1016/j.jag.2012.12.008.

Sellier, V., O. Navratil, J. P. Laceby, M. Allenbach, I. Lefèvre, and O. Evrard. 2021. "Reconstructing the Impact of Nickel Mining Activities on Sediment Supply to the Rivers and the Lagoon of South Pacific Islands: Lessons Learnt from the Thio Early Mining Site (New Caledonia)." *Geomorphology* 372: 107459–107459. https://doi.org/10.1016/j.geomorph.2020.107459.

Sun, S., L. Liu, J. Hu, and H. Ding. 2022. "Failure Characteristics and Mechanism of a Rain-Triggered Landslide in the Northern Longwall of Fushun West Open Pit, China." *Landslides* 19 (10): 2439–2458. https://doi.org/10.1007/s10346-022-01926-3.

Wang, S., Z. Bai, Y. Lv, and W. Zhou. 2022. "Monitoring Extractive Activity-Induced Surface Subsidence in Highland and Alpine Opencast Coal Mining Areas with Multi-Source Data." *Remote Sensing* 14 (14): 3442–3442. https://doi.org/10.3390/rs14143442.

Wu, Q., C. Song, K. Liu, and L. Ke. 2020. "Integration of Tandem-X and SRTM DEMs and Spectral Imagery to Improve the Large-Scale Detection of Opencast Mining Areas." *Remote Sensing* 12 (9): 1451–1451. https://doi.org/10.3390/rs12091451.

Yan, Y., X. Ling, F. Zhang, and J. Wang. 2013. "Stability and Deformation Analysis for Excavation and Backfilling of Fushun West Open-Pit Coal Mine." *Applied Mechanics and Materials* 353-356: 751–755. https://doi.org/10.4028/www.scientific.net/AMM.353-356.751.

Yang, S., J. Zhang, Y. Chen, and Z. Song. 2016. "Effect of Upward Angle on the Drawing Mechanism in Longwall Top-Coal Caving Mining." *International Journal of Rock*

Mechanics and Mining Sciences 85: 92–101. https://doi.org/10.1016/j.ijrmms.2016.03.004.

Yang, Z., Z. Li, J. Zhu, Y. Wang, and L. Wu. 2020. "Use of SAR/InSAR in Mining Deformation Monitoring, Parameter Inversion, and Forward Predictions: A Review." *IEEE Geoscience and Remote Sensing Magazine* 8 (1): 71–90. https://doi.org/10.1109/MGRS.2019.2954824.

Zhang, F., T. Yang, L. Li, Z. Wang, and P. Xiao. 2019. "Cooperative Monitoring and Numerical Investigation on the Stability of the South Slope of the Fushun West Open-Pit Mine." *Bulletin of Engineering Geology and the Environment* 78 (4): 2409–2429. https://doi.org/10.1007/s10064-018-1248-z.

Zhou, C., Y. Cao, X. Hu, K. Yin, Y. Wang, and F. Catani. 2022. "Enhanced Dynamic Landslide Hazard Mapping Using MT-InSAR Method in the Three Gorges Reservoir Area." *Landslides* 19 (7): 1585–1597. https://doi.org/10.1007/s10346-021-01796-1.